Inorganic Chemistry

β-Irradiation Effects on the Formation and Stability of CaMoO₄ in a Soda Lime Borosilicate Glass Ceramic for Nuclear Waste Storage

Karishma B. Patel,*,†,‖ Bruno Boizot,‡,△ Sébastien P. Facq,† Giulio I. Lampronti,† Sylvain Peuget,§ Sophie Schuller,⊥ and Ian Farnan†

†Department of Earth Sciences, University of Cambridge, Downing Street, Cambridge CB23EQ, U.K.
‡Ecole Polytechnique, Laboratoire des Solides Irradiés, CEA/DSM/IRAMIS, CNRS, 91128 Palaiseau Cedex, France
§CEA, DEN, DTCD, SECM, LMPA, Marcoule, F-30207 Bagnols-sur-Cèze, France
⊥CEA, DEN, DTCD, SCDV, LDPV, Marcoule, F-30207 Bagnols-sur-Cèze, France

S *Supporting Information*

ABSTRACT: Molybdenum solubility is a limiting factor to actinide loading in nuclear waste glasses, as it initiates the formation of water-soluble crystalline phases such as alkali molybdates. To increase waste loading efficiency, alternative glass ceramic structures are sought that prove resistant to internal radiation resulting from radioisotope decay. In this study, selective formation of water-durable $CaMoO_4$ in a soda lime borosilicate is achieved by introducing up to 10 mol % MoO_3 in a 1:1 ratio to CaO using a sintering process. The resulting homogeneously dispersed spherical $CaMoO_4$ nanocrystallites were analyzed using electron microscopy, X-ray diffraction (XRD), Raman and electron paramagnetic resonance (EPR) spectroscopies prior to and post irradiation, which replicated internal β-irradiation damage on an accelerated scale. Following 0.77 to 1.34 GGy of 2.5 MeV electron radiation $CaMoO_4$ does not exhibit amorphization or significant transformation. Nor does irradiation induce glass-in-glass phase separation in the surrounding amorphous matrix, or the precipitation of other molybdates, thus proving that excess molybdenum can be successfully incorporated into a structure that it is resistant to β-irradiation proportional to 1000 years of storage without water-soluble byproducts. The $CaMoO_4$ crystallites do however exhibit a nonlinear Scherrer crystallite size pattern with dose, as determined by a Rietveld refinement of XRD patterns and an alteration in crystal quality as deduced by anisotropic peak changes in both XRD and Raman spectroscopy. Radiation-induced modifications in the $CaMoO_4$ tetragonal unit cell occurred primarily along the c-axis indicating relaxation of stacked calcium polyhedra. Concurrently, a strong reduction of Mo^{6+} to Mo^{5+} during irradiation is observed by EPR, which is believed to enhance Ca mobility. These combined results are used to hypothesize a crystallite size alteration model based on a combination of relaxation and diffusion-based processes initiated by added energy from β-impingement and second-order structural modifications induced by defect accumulation.
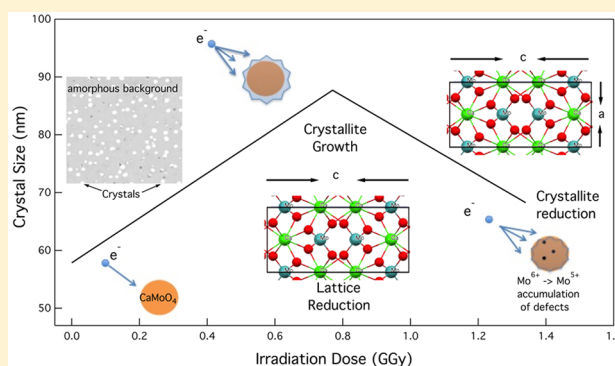
1. INTRODUCTION

Vitrification into a borosilicate glass is a widely accepted technique to immobilize nuclear waste. Amorphous structures are ideal waste form candidates, as they are able to incorporate a wide array of nuclides, show resistance to internal radiation, and have fairly good chemical stability when subjected to aqueous environments.[1−3] These properties are dependent on the glass remaining single-phased and fully amorphous, which limits the nuclear waste loading to 18.5 wt % in the French nuclear waste glass R7T7.[4,5]

One of the limiting factors to waste loading is the concentration of MoO_3, as molybdenum has a low solubility in silicate and borosilicate glasses.[5,6] Molybdenum can exist in several oxidation states (Mo^{6+}, Mo^{5+}, Mo^{4+}, Mo^{3+}), but in oxidizing or neutral conditions Mo ions are considered to be primarily hexavalent, taking the form of $[MoO_4]^{2−}$ tetrahe-

dra.[7−9] These tetrahedra are found to be unconnected to the glassy framework and are located in nonbridging oxygen (NBO) channels containing alkali and alkaline earth deposits.[9−11] The $[MoO_4]^{2−}$ tetrahedral form of molybdenum is found in both the glassy and crystalline phases, which could account for its low solubility in borosilicates. In R7T7 this limit is 1 mol % for a cooling rate of 1 °C·min⁻¹, but it can be increased to 2.5 mol % if the melt is rapidly quenched at 1×10^4 °C·min⁻¹.[12]

When the solubility of molybdenum is exceeded it could initiate the precipitation of alkali molybdates (Na_2MoO_4) during glass synthesis.[11,13] These molybdates along with chromates are highly water-soluble and can act as carriers of

radioactive cesium, strontium, or minor actinides.[1,14] These complexes are known as yellow phase and can severely alter the safety case for geological deposition of nuclear waste forms by increasing corrosion tendencies.[6,9,11] Not only will the formation of molybdates alter chemical durability, but uncontrolled crystallization can also lead to swelling and eventual cracking at the glass-crystal interface.[15] This phenomenon can be accentuated by internal radiation, as this can create additional strain within the system.[16]

Investigations into alternative material compositions are led by a desire to increase waste loading to decrease the final number of canisters for storage and to accommodate higher burn-up waste. High-level waste (HLW) streams with a higher concentration of Mo, namely, legacy waste arising from U−Mo fuel, are concurrent contributors to research motivation.[6,17,18] Ceramic alternatives based on natural analogues have been proposed for some HLW streams, but they require high temperature and pressure during fabrication, making them both costly and time-consuming to manufacture. Another option of interest is glass ceramic (GC) materials. GCs are a useful alternative, as they utilize an amorphous matrix to encapsulate the majority of shorter-lived radioisotopes but enable actinides and poorly soluble waste components such as sulfates, chlorides, and molybdates to be contained in a more durable crystalline phase without significantly alternating the physiochemical properties of the waste form.[1,17]

Essential studies are underway to only initiate the crystallization of water-durable phases that are compatible with the surrounding matrix and show high radiation resistance. Powellite ($CaMoO_4$) is one such candidate. Selective formation of $CaMoO_4$ can be driven by several factors including composition, external heat treatments, redox conditions, or fabrication techniques.[5,10,19,20] Rapidly quenching the system and reducing conditions will both affect Mo solubility,[22] rather than speciation directly, whereas composition plays a complex role in initiating crystallization and determination of precipitates. To begin with, the preference of charge compensators will have a significant impact on speciation. Both $[BO_4]^-$ and $[MoO_4]^{2-}$ entities prefer to be charge-balanced by Na^+ ions owing to the size, charge, and mobility of the ion, but $[BO_4]^-$ units have a higher affinity toward Na^+ ions.[23] If Na^+ ions are engaged in charge compensation of network formers, then $[MoO_4]^{2-}$ and Ca^{2+} ions will consequently initiate nucleation of $CaMoO_4$.[21,8,11] This trend has been observed to increase when the concentration of CaO or B_2O_3 in the initial glass composition is increased, as it affects the population of $[BO_4]^-$ species.[5,10] Furthermore, the inclusion of rare earths can also significantly affect $CaMoO_4$ crystallization. Adding Nd_2O_3 to a glass has been observed to increase the solubility of molybdenum and inhibit crystallization of molybdates by increasing disorder in the depolymerized region, where $[MoO_4]^{2-}$ entities and cationic charge balancers are found.[7]

While speciation of molybdates during synthesis has been thoroughly investigated, the affects of radiation are less well-understood. During storage, nuclear waste will constantly undergo both α- and β-decay within its containment material. Radiation damage is known to cause atomic displacements, ionization, and electronic excitations within a waste containment structure. These effects can macroscopically lead to swelling or densification, defect-induced cracking,[24] or phase separation,[16,25,26] thus proving potentially problematic.

To emulate inelastic collisions caused by self-irradiation, external β-irradiation can be used to replicate long-term damage. Borosilicate glasses under β-irradiation exhibit several structural changes for an integrated dose greater than or equal to 1×10^9 Gy, which is consistent with the accumulated dose received following 1000 years of storage. The primary modifications observed are (i) the radiolysis of bonds to create punctual defects[27,28] that can lead to the production of molecular oxygen;[29] (ii) the reduction of rare earths and transitional metals;[30,31] (iii) the clustering of alkalis and other charge compensators;[2,32] (iv) changes to the coordination of network formers that can lead to an increase in the polymerization[33] or phase separation of the glassy matrix at higher doses;[34] and (v) changes in glass properties such as an increase in plasticity.[35]

We demonstrate in this paper how these radiation-induced structural modifications present themselves in GCs and investigate subsequent effects on $CaMoO_4$ nucleation and stability. This study aims to test the hypothesis of whether β-irradiation will induce phase separation in homogeneous systems, incite local amorphization of crystalline phases, or propagate existing separative phases initiated during synthesis.

2. EXPERIMENTAL SECTION

2.1. Glass Preparation. In this study we prepared several nonactive samples to selectively form $CaMoO_4$ by increasing the concentration of MoO_3 in a 1:1 ratio to CaO in a borosilicate glass normalized to SON68 (nonactive form of R7T7) with respect to SiO_2, B_2O_3, and Na_2O. Excess CaO was required for powellite formation but was carefully investigated, as it is known to cause glass-in-glass phase separation when greater than 11 mol %.[21] Two simplified soda and soda lime borosilicates were also prepared to test the glass-in-glass phase separation tendencies without molybdenum and to isolate the effects of cations on network formers.

Four of the samples (labeled CNG) included 0.15 mol % Gd_2O_3, which acted as a spectroscopic probe for electron paramagnetic resonance (EPR) measurements. Rare earths can also be considered actinide surrogates. They therefore act as a marker for the incorporation of active species in either the glassy or crystalline phase. An additional sample containing MoO_3, but without Gd_2O_3, was also included to identify the effects of minor dopants on crystallization. Table 1 provides the normalized compositions synthesized in this investigation.
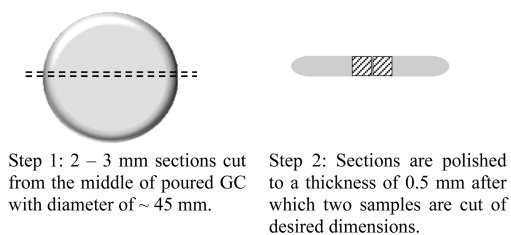
Table 1. Sample Compositions (in mol %)

sample	SiO_2	B_2O_3	Na_2O	CaO	MoO_3	Gd_2O_3
NaBSi	70.00	18.50	11.50			
CNO	63.39	16.88	13.70	6.03		
CNG1	61.94	16.49	13.39	7.03	1.00	0.15
CNG1.75	60.93	16.22	13.17	7.78	1.75	0.15
CNG2.5	59.93	15.96	12.95	8.52	2.50	0.15
CNG7	53.84	14.34	11.64	13.03	7.00	0.15
CN10	49.90	13.29	10.78	16.03	10.00	

Glass batches of ~30 g were prepared from melting SiO_2, H_3BO_3, $Na_2B_4O_7$, Na_2CO_3, $CaCO_3$, MoO_3, and Gd_2O_3 powders at atmosphere in a platinum/ruthenium crucible at 1500 °C for 30 min. Samples were crushed and remelted at 1500 °C for 20 min to ensure homogeneity of element distribution. Melts were then cast at room temperature on a graphite-coated iron plate and annealed for 24 h at 520 °C.

Samples were cut to an average thickness of 500 μm to ensure homogeneous β-irradiation throughout the sample volume and were roughly 3 mm× 3 mm in surface dimensions to fit the beamline sample holder. Sample surfaces were hand-polished using SiC polishing paper, grades P320, P600, P800, P1200, P2400, and P4000, followed by 3 and 1 μm diamond polishing using a dimple grinder.

Three pieces were cut from each glass batch. Two were irradiated, and the third served as a reference for alteration and is referred to as the "pristine" sample. All three specimens were taken from the center of the rod to mitigate the effects of location-based cooling on crystallization during synthesis (see Figure 1). Furthermore, the

Step 1: 2 – 3 mm sections cut from the middle of poured GC with diameter of ~ 45 mm.

Step 2: Sections are polished to a thickness of 0.5 mm after which two samples are cut of desired dimensions.

Figure 1. Schematic of sampling technique used to select sections for analysis and experimentation from bulk.

"pristine" monolith was compared to powder X-ray diffraction (XRD) of poured samples to ensure that the crystal content and quality of the reference specimen represented the bulk.

2.2. Irradiation Experiment. Electron irradiation is usually used to replicate the damage observed following β-decay within a radioactive material.[16] The β-irradiation in this experiment was performed with 2.5 MeV electrons from the Pelletron accelerator (SIRIUS facility) at LSI in France. To keep the maximum temperature of the sample holder at 50 °C and thus negate temperature effects, an average current of 15.8 μA was used. With these beam specifications, doses of 0.77 and 1.34 GGy were achieved on two sample sets (see Figure 2). These doses are within an order of magnitude consistent with 1000 years of storage for 18.5 wt % waste loading,[16,17] thus representing long-term modification.
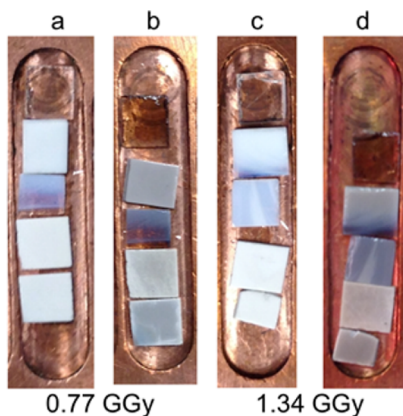
Figure 2. Samples CNG1 (top), CNG1.75, CNG2.5, CNG7, and CN10 (bottom) in a Cu sample holder. For dose of 0.77 GGy: (a) monoliths prior to irradiation; (b) post irradiation. For samples subjected to a dose of 1.34 GGy: (c) prior to irradiation; (d) following irradiation.

2.3. Characterization Techniques. Sample morphology and crystal phase determination were investigated using XRD and scanning electron microscopy (SEM). These techniques combined were able to determine changes to crystallite size, texture, and distribution as a function of dose.

Visual changes in phase separation were determined through SEM backscattered (BS) mapping performed on a Quanta-650F at low vacuum (0.06−0.08 mbar) with a 5 keV beam resulting in a penetration depth of ~1 μm. Energy-dispersive X-ray analysis (EDS) was likewise performed at low vacuum but with a 7.5−20 keV beam using an 8 mm cone to reduce skirting effects. EDS was used to determine the relative composition of crystals and the residual glass. However, boron concentrations could not be determined, as it is

below detection limits and oxygen was not measured directly but was determined by stoichiometric oxide ratios.

XRD was performed with Cu $K\alpha_1$ ($\lambda = 0.154\,06$ nm) and Cu $K\alpha_2$ ($\lambda = 0.154\,44$ nm) wavelengths on a Bruker D8 ADVANCE equipped with Göbel mirrors for a parallel primary beam and a Vautec position-sensitive detector. Spectra were collected for $2\theta = 10−90°$ with a 0.02° step size. Samples were analyzed as monoliths to isolate irradiation effects and avoid structural modifications induced by the mechanical force required to powder samples, but they were rotated to identify the maximum diffracting angle of incidence. Crystal size (CS) estimates were then determined from Rietveld refinements of whole XRD patterns, which incorporated the Scherrer eq 1:

$$\text{crystal size(CS)[nm]} = k\lambda/(10 \cdot \Delta\theta \cdot \cos\theta) \tag{1}$$

where k is a crystal shape factor (assumed to be 0.9), λ is the radiation wavelength, and θ is the diffraction angle. This equation was applied to the peak shape function in a given crystallographic direction (hkl) according to the following relationship (eq 2):

$$\text{fwhm}(2\theta, hkl) = (180/\pi)\lambda/(\cos\theta \cdot \text{CS}) \tag{2}$$

where fwhm(2θ) is the full width at half-maximum of a peak at a given diffraction angle and crystallographic direction.[36] The LaB$_6$ 660b NIST standard[37] was used to model the instrumental contribution to peak broadening using a fundamental four-parameter approach with the software Topas v4.1.[38] Peaks were fit using Lorentzian functions and modeled assuming isotropic variation. A Scherrer CS-only analysis was employed, as the correlation between size and strain was too high (see Supporting Information).

Raman spectroscopy was utilized to determine relative changes induced by irradiation in both the amorphous and crystalline phases. Spectra were measured on a confocal LabRam300 Horiba Jobin Yvon spectrometer using a 532 nm laser produced by a diode-pumped solid-state laser with incident power of 100 mW. Measurements were collected with a 300 μm confocal hole size and used an Olympus 50× objective with a holographic grating of 1800 mm^{-1}, coupled to a Peltier-cooled front-illuminated CCD detector over the range from 150 to 1600 cm^{-1} with a 2 μm spot size. Depth profile analysis was used to estimate a penetration depth of ~22 μm in such a configuration. Spectra were analyzed using PeakFit software, and the CaMoO$_4$ characteristic bands were fit with pseudovoigt profiles. Three sites were probed per sample, and average values were used for peak analysis.

EPR was used to describe the defect structure in the bulk of both crystalline and amorphous phases. EPR spectra were collected at the X-band ($\nu \approx 9.86$ GHz) on an EMX Bruker spectrometer at room temperature with 100 kHz field modulation and 1 mW microwave power using quartz tubes. All EPR spectra are normalized to the relative sample weight, modulator attenuation, and receiver gain.

3. RESULTS

3.1. Microstructure of Pristine Samples. With the given synthesis and cooling conditions, the molybdenum solubility limit in this soda lime borosilicate is below 1.75 mol % MoO$_3$, as determined by optical analysis and examination of SEM micrographs. Below the solubility limit samples were characterized with a homogeneous gray surface by SEM (see Supporting Information) and were optically transparent (see Figure 2, top row). This result agrees with studies performed for simplified soda lime borosilicates enriched with MoO$_3$.[21,8,39,40] In addition to CNG1, simplified glasses NaBSi and CNO were also single-phased by microscopy. Additionally, no diffraction peaks or crystal bands were identifiable by either XRD or Raman analysis.

Between 1.75 and 2.5 mol % MoO$_3$, samples display a visible opalescence, and SEM imaging reveals the precipitation of homogeneously dispersed spherical particles ~180−430 nm in diameter (see Figure 3) comprised of crystallites between 50
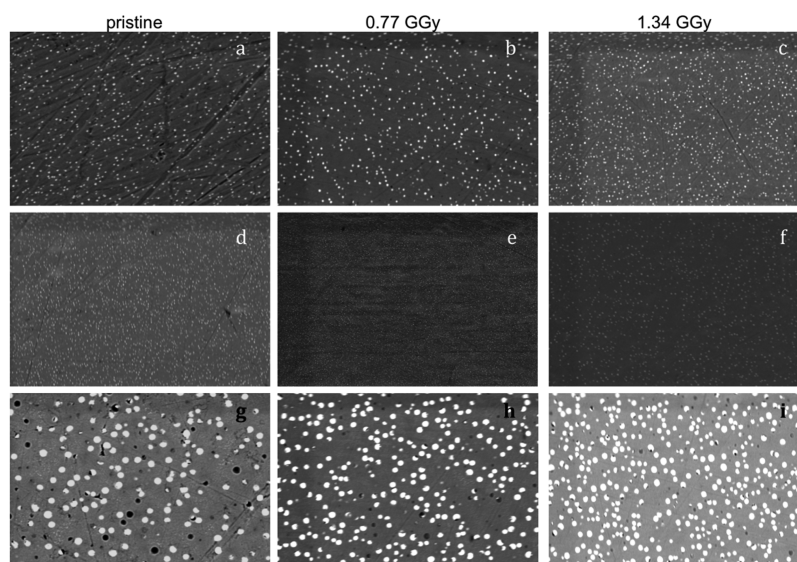
Figure 3. SEM BS micrographs scaled to 20 μm × 30 μm. (a) Pristine CNG1.75; (b) CNG1.75 irradiated to 0.77 GGy: particles appear somewhat larger; (c) CNG1.75 irradiated to 1.34 GGy: particles look similar in size to pristine sample (a); (d) pristine CNG2.5 (e) CNG2.5 irradiated to 0.77 GGy: shows smaller crystallites than in pristine sample (d); and (f) CNG2.5 irradiated to 1.34 GGy; (g) pristine CNG7; (h) CNG7 irradiated to 0.77 GGy; and (i) CNG7 irradiated to 1.34 GGy.

Table 2. Crystallite Size in Diameter and Cell Parameters[a] from Rietveld Refinement of XRD Spectra using TOPAS

sample ID	CS (nm) pristine	a (Å)	c (Å)	CS (nm) 0.77 GGy	a (Å)	c (Å)	CS (nm) 1.34 GGy	a (Å)	c (Å)
CNG1.75	51.27	5.2289	11.4605	84.94	5.2263	11.4474	69.06	5.2246	11.4441
	(±2.26)	(±0.0011)	(±0.0034)	(±3.25)	(±0.0045)	(±0.0014)	(±2.34)	(±0.0005)	(±0.0017)
CNG2.5	55.09	5.2280	11.4593	44.38	5.2279	11.4512	56.17	5.2261	11.4478
	(±2.08)	(±0.0008)	(±0.0025)	(±2.68)	(±0.0014)	(±0.0047)	(±2.31)	(±0.0008)	(±0.0027)
CNG7	143.38	5.2265	11.4558	186.13	5.2265	11.4466	159.36	5.2257	11.4440
	(±2.54)	(±0.0001)	(±0.0003)	(±4.69)	(±0.0001)	(±0.0003)	(±3.42)	(±0.0001)	(±0.0003)
CN10	125.24	5.2264	11.4554	130.97	5.2256	11.4478	118.53	5.2257	11.4402
	(±1.94)	(±0.0001)	(±0.003)	(±4.13)	(±0.0002)	(±0.0007)	(±3.00)	(±0.0002)	(±0.0006)

[a]Estimated standard deviation for each parameter given in brackets.

and 55 nm in diameter, as determined by XRD. The blue coloration seen in CNG1.75 and CNG2.5 (Figure 2) is attributed to the presence of gadolinium, and its optical luminescence is correlated to the level of powellite crystallization. Increasing the concentration of MoO_3 to 7 mol % caused the glasses to become more opaque. Correspondingly crystallites grew up to ~140 nm in diameter, and particles grew up to 0.5−1.0 μm in diameter (Tables 2 and 3). This transition indicates an increasing fraction of liquid−liquid phase separation in proportion to $[MoO_3]$.

Samples CNG1.75, CNG2.5, CNG7, and CN10, exhibiting nanocrystallites that aggregated into particles less than or equal to 1 μm, showed diffraction patterns for a single phase identified as a tetragonal scheelite-type powellite ($CaMoO_4$) structure with an $I4_1/$ space group (see Figure 4). In this structure, $[MoO_4]^{2-}$ tetrahedra are charge-balanced by eight-fold coordinated calcium. The tetragonal cell parameters of powellite determined by Rietveld refinements of XRD spectra range between a = 5.226−5.229 Å and c = 11.455−11.460 Å. Increasing the initial concentration of MoO_3 is observed to decrease the cell parameters and generally increase the CS according to a decrease in diffraction peak broadening; see Table 2. A small discrepancy arises in CN10, in which the CS is ~15 nm smaller than they are in CNG7, despite having an additional 3 mol % of MoO_3. However, the range of particle

Table 3. Estimated Range of Bimodal Particle Sizes Observed on SEM Micrographs for GCs As Observed in Figure 3 and through High-Resolution Imaging in Figure 7

sample ID	PS (nm) pristine	PS (nm) 0.77 GGy	PS (nm) 1.34 GGy
CNG1.75	257−429	228−319	173−246
	~60[a]	~60[a]	−
CNG2.5	185−295	64−100	109−164
	−	−	−
CNG7	528−950	593−866	383−739
	~140[a]	~140[a]	~140[a]
CN10	703−1000	603−1095	656−1003
	~130[a]	~130[a]	~130[a]

[a]Small particle estimates are assumed constant owing to resolution limitations of the equipment at this scale, but a variation likely exists that corresponds to crystallite size. A dash indicates that no smaller particles were observed.

sizes (PS) detected by SEM for both samples is similar (see Table 3). This is therefore presumed to be a result of Gd_2O_3 doping.

All particles in Figure 3 are evenly distributed throughout the sample. In general we can detect two groups of PS. One is in the range of 200−400 nm for $MoO_3 \leq 2.5$ mol %, and the other is in the range of 0.5−1.0 μm for $MoO_3 \geq 7$ mol %.
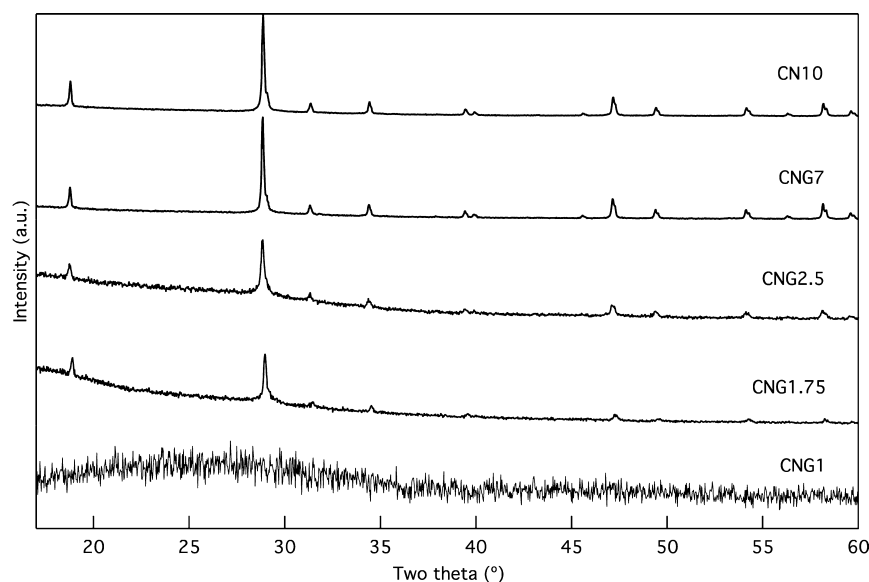
Figure 4. Raw XRD spectra of pristine samples with increasing concentration of MoO_3. In ascending order: 1.0 mol %, 1.75 mol %, 2.5 mol %, 7 mol %, and 10 mol % MoO_3. CNG1 is fully amorphous, and all diffraction peaks in other spectra are associated with a single-crystal phase of $CaMoO_4$ (synthetic). Halo in diffractogram ~22° is a signature of the amorphous phase.

These ranges correspond to CS less than 85 nm and those greater than 120 nm, respectively. This result indicates an apparent correlation between the CS and PS in pristine samples.

While images and CS values for GCs with 1.75−2.50 mol % MoO_3 are very similar (see Figure 3 and Table 3), high-resolution image analysis actually indicates that the smallest crystal aggregates are found in CNG2.5. This result is supported by the largest amorphous contributions for CNG2.5 using Raman spectroscopy.

The diffraction results on crystal-phase determination were supported by EDS analysis (see Supporting Information), which indicates Ca and Mo form clusters and Na remains in the matrix. EDS analysis also shows that Si and Na are uniformly dispersed in the matrix, implying that the glassy framework is fairly homogeneous, as Na atoms are indicative of boron distribution.

3.2. Microstructure of Irradiated Samples. Following irradiation, glasses and GCs experienced macroscopic discoloration; see Figure 2b,d. A reduction caused fully amorphous samples to obtain a brown tint, while GCs resulted in visible greying at the surface. Microscopically, glasses that were completely amorphous at pristine conditions remained so following irradiation according to XRD and SEM.

For GCs the morphology of the crystalline phase remained spherical in nature and evenly distributed. XRD patterns of samples containing greater than 1 mol % MoO_3 still exhibited only a single powellite phase following irradiation. EDS analysis confirmed this result with no significant Na substitution into molybdates (Figure 5). Furthermore, quantitative analysis indicates that the Mo/Ca ratio in precipitates increases from ~0.81 to ~0.86 (±0.05−0.06) following irradiation for high $[MoO_3]$. This result alludes to a migration of Ca atoms away from crystal centers or a decreased solubility of molybdenum. This change is concurrent to a 0.2−0.3 (±0.15) mol % increase of Mo relative to Ca in the glassy matrix indicative of increased Mo solubility following a dose of 1.34 GGy. While a similar pattern was observed in all GCs, the change falls within the propagated error and may therefore be an artifact.
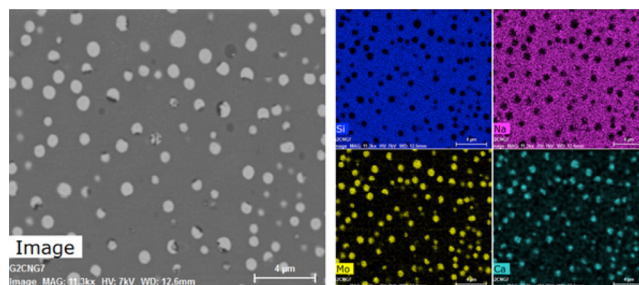
Figure 5. EDS mapping of CNG7 irradiated with a dose of 1.34 GGy confirms the formation of Ca−Mo crystallites generally free of Na substitutions. Micrograph dimensions: 20.8 μm × 17.6 μm. Blue: Si (top left); pink: Na (top right); yellow: Mo (bottom left); aqua: Ca (bottom right).

For $[MoO_3] \leq 2.5$ mol % when crystallites are ~50 nm, EDS analysis indicates an excess of calcium near Mo centers with Mo/Ca ≈ 0.4 for CNG2.5 and ~0.56 for CNG1.75 prior to and following irradiation. The Mo/Ca variation between high and low $[MoO_3]$ samples is likely a result of the large electron-beam spot size used for quantification. For particle sizes less than 300 nm the electron beam scatters both the precipitate and the area surrounding the particles. The higher relative amount of Ca therefore indicates that a cationic sublattice surrounds crystalline molybdates.

XRD analysis revealed that irradiation caused an anisotropic reduction in the cell parameters a and c, while maintaining a tetragonal unit cell. At the first dose of 0.77 GGy the c cell parameter rapidly reduces and then tails off at 1.34 GGy (see Figure 6). A clear relationship between the a cell parameter and dose is difficult to determine owing to the large statistical error in refinement of this parameter. This is particularly prevalent in samples with a low concentration of MoO_3 (≤ 2.5 mol %), as the amorphous contribution at low angles of 2θ causes some peak distortion. In general, CNG1.75 and CN10 have one trend, and CNG2.5 and CNG7 have another. In the first group, the rate of change in a is greater at 0.77 GGy than at 1.34 GGy, whereas in the latter group it is almost the same at 0.77 GGy as
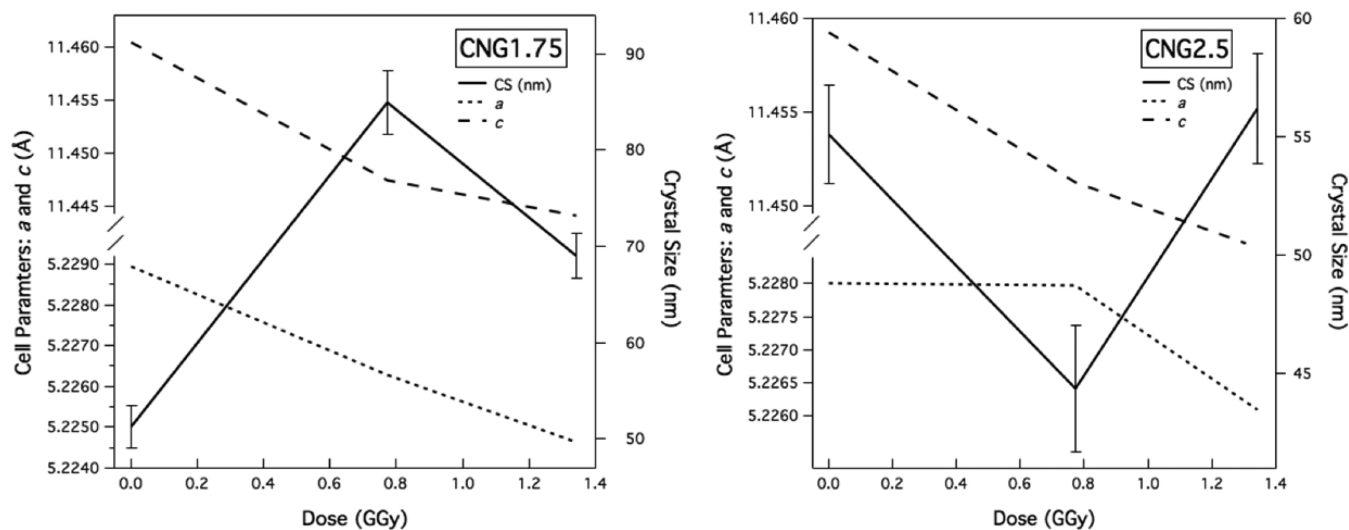
Figure 6. Visualizations of changes in cell parameters (left axis) and Scherrer crystallite size (right axis) as estimated by Rietveld refinement of XRD patterns in CNG1.75 and CNG2.5, which show opposing trends in CS. Note error bars were not included for the cell parameters, but the relevant estimated standard deviation is provided in Table 2.

pristine conditions before dropping off at 1.34 GGy. Despite these variations and large estimated standard deviation in low MoO_3 bearing GCs, the a cell parameter is always smaller following β-irradiation. These results can be found in Table 2 and indicate that irradiation causes a relaxation or compression of the unit cell. As the magnitude of change is larger in the c direction than for a in all compositions, we can assume that irradiation predominantly alters the order of stacked Ca polyhedra along the c axis relative to changes in the Mo−O bonds that would affect Mo polyhedra stacking in the a axis.

Though the cell parameters experience a decrease in value following β-irradiation at any dose, the Scherrer CS exhibits an unusual growth trend. For CNG1.75, CNG7, and CN10 the average CS increases by ~30, 40, and 15 nm in diameter, respectively, following a dose of 0.77 GGy. This increase in CS corresponds to a decrease in peak broadening. Doubling the dose to 1.34 GGy results in a subsequent reduction of CS to range closer to unirradiated samples, corresponding to a subsequent increase in the fwhm. An anomaly occurs in CNG2.5, where the opposite trend in CS is observed. At 0.77 GGy there is a reduction by ~10 nm, and at a higher dose, CS once again recovers to roughly pristine specifications (see Figure 6). It is interesting to note that CNG2.5 displays the smallest crystals following irradiation, though at pristine conditions they are similar in size to CNG1.75.

Qualitative observations on separated phases were easily made from SEM images, where the crystalline phase (or particles) is in high contrast to the amorphous phase. Using this methodology, we can infer that irradiation causes a change in the range and distribution of PS at the sample surface. In CNG1.75 and CNG7 the mode PS may increase at 0.77 GGy (see Figure 3), but the range of PS as a whole decreases (see Table 3) with dose suggesting a change in PS distribution. These combined results indicate a decrease in overall phase separation but a growth of select particles.

At higher resolution we can observe a spattering of smaller particles 60−140 nm in diameter throughout the matrix of GCs prior to irradiation (see Figure 7) that approach CS values. Following a dose of 1.34 GGy there are far fewer of these smaller particles in all GCs, and none are detected in CNG2.5
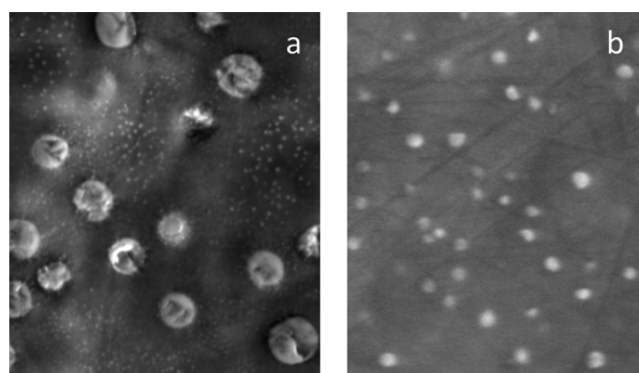

Figure 7. SEM micrographs of (a) CNG7 (7.9 μm × 6.7 μm) show several large spherulites (>500 nm) and a spattering of much smaller (~140 nm) particles in the matrix; and (b) CNG2.5 (3.5 μm × 3.0 μm) that only have one size of particles (~140 nm).

or CNG1.75. In fact no small particles are detected in CNG2.5 before (Figure 7) or after irradiation, which could indicate that the distribution of PS increases in proportion to CS. It could also indicate that the CS alteration observed in this composition is influenced by a more uniform nucleation and growth process during synthesis and hence more uniform distribution in PS. The reduction of smaller particles following irradiation indicates either migration along NBO channels, dissolution into the matrix, or growth into larger particles despite a global reduction in PS distribution with dose. The results further indicate that there is no nucleation of $CaMoO_4$ particles in any of the samples, as the number of smaller particles decreases.

3.3. Raman Analyses. *3.31. Pristine Samples.* As previously mentioned, Raman spectroscopy can be used to elucidate the structure of the crystalline phase, as well as short-range order in the amorphous phase. Each Raman band represents a distinct collection of vibration modes for elastic, periodically arranged atoms or molecules in matter.[41] Therefore, changes to peak area, position, or line width are representative of changes in the level of disorder in the system. According to Group Theory, the lattice vibrations for powellite can be divided into 26 species of even and odd vibrations for
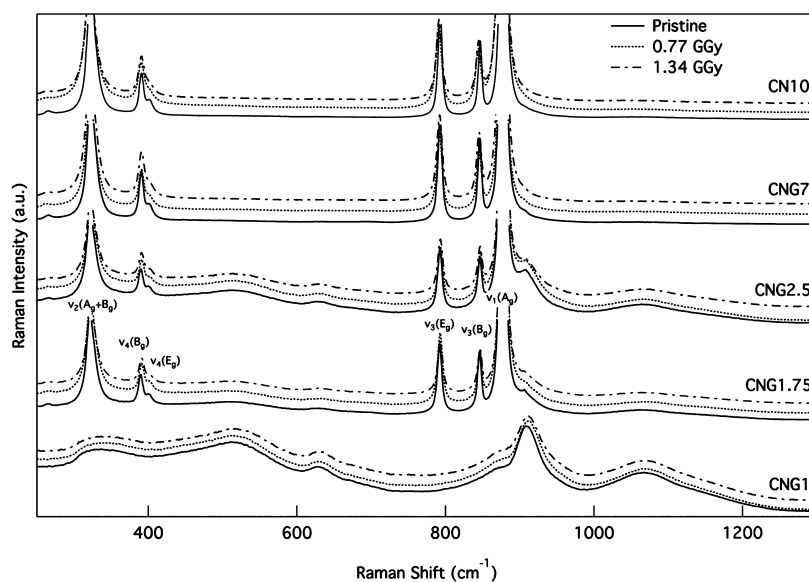
Figure 8. Raman spectra of pristine, 0.77 GGy, and 1.34 GGy β-irradiated samples with increasing concentraion of MoO_3. In ascending order: 1, 1.75, 2.5, 7, and 10 mol % MoO_3. The internal modes of $[MoO_4]^{2-}$ tetrahedron in powellite are $\nu_1(A_g)$ 878 cm^{-1}, $\nu_3(B_g)$ 848 cm^{-1}, $\nu_3(E_g)$ 795 cm^{-1}, $\nu_4(E_g)$ 405 cm^{-1}, $\nu_4(B_g)$ 393 cm^{-1}, and $\nu_2(A_g+B_g)$ 330 cm^{-1} and are labeled on the plot.
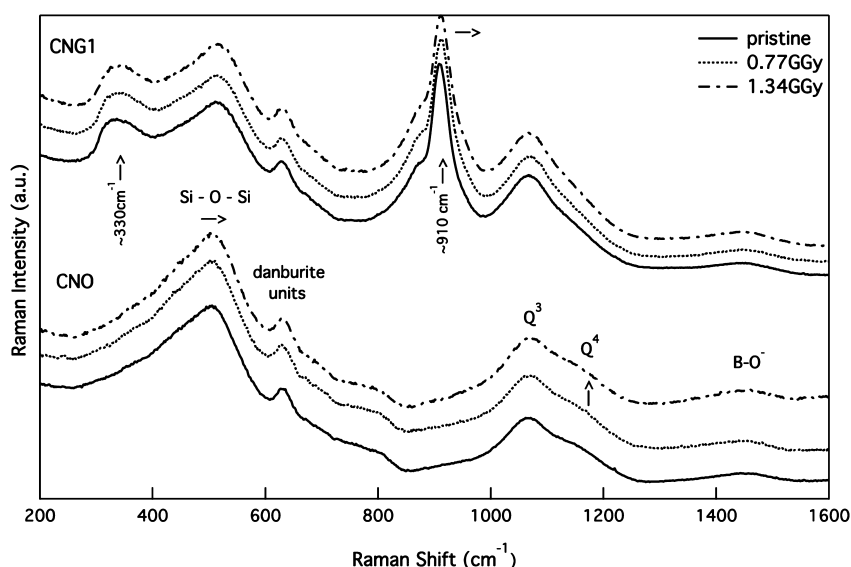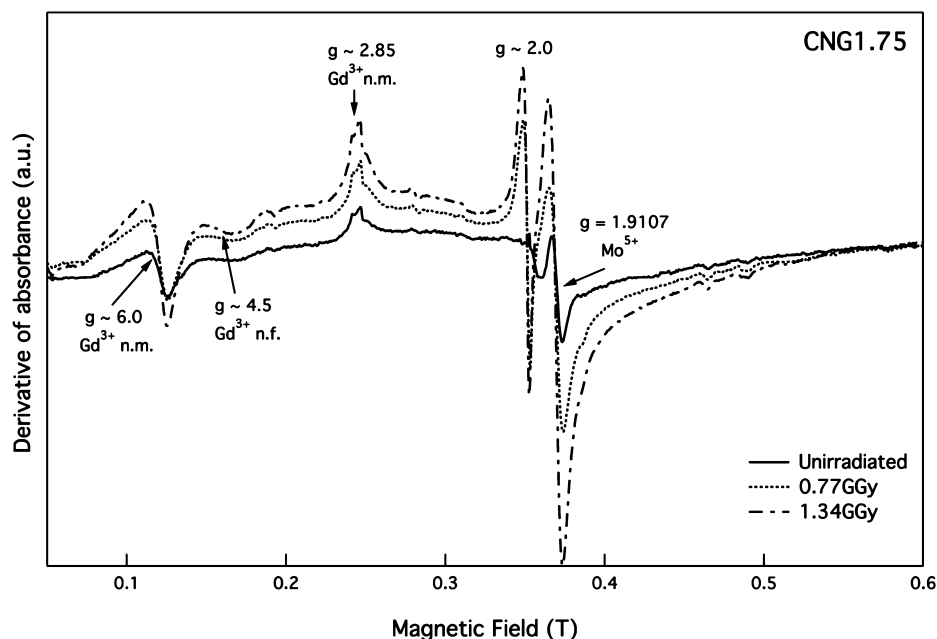

Figure 9. Raman spectra of pristine, 0.77 GGy, and 1.34 GGy β-irradiated CNO and CNG1 illustrating the effects Mo inclusion in an amorphous structure.

C_{4h} point symmetry, the latter of which are Raman-active.[41] The relevant visible internal $[MoO_4]^{2-}$ modes in powellite are symmetric elongation of the molybdenum tetrahedra $\nu_1(A_g)$ 878 cm^{-1}, unsymmetrical translation of double degenerate modes $\nu_3(B_g)$ 848 cm^{-1}, $\nu_3(E_g)$ 795 cm^{-1}, $\nu_4(E_g)$ 405 cm^{-1}, symmetric bending $\nu_4(B_g)$ 393 cm^{-1}, and unsymmetrical bending $\nu_2(A_g+B_g)$ 330 cm^{-1}. These modes are observable in Figure 8 for glass ceramics with $[MoO_3] \geq 1$ mol % at pristine conditions.[42,43] Additionally, there are three external modes at 206, 188, and 141 cm^{-1} (not shown in this paper) assigned to translational modes of Ca–O and MoO_4.[42] These are formally considered $\nu_{def}(A_g)$ deformation modes of the cationic sublattice.[44]

The peak position of the internal $[MoO_4]^{2-}$ modes experiences a shift of ∼0.4−0.8 cm^{-1} to higher wavenumbers, as the concentration of MoO_3 increases from 1.75−7 mol %

(see Supporting Information), which corresponds to a growth in CS from ∼50 to 140 nm (Table 2). This shift could therefore be related to the degree of phase separation or crystallite growth within separated phases. The observed peak positions in all GCs are at a lower wavenumber than the internal modes listed for single-crystal powellite.[42,43] As the concentration of MoO_3 increases, the peak position moves closer to theoretical values at higher wavenumbers, and the cell parameters correspondingly decrease. In addition to a marginal change in position, the peak fwhm also changes. It is observed to decrease in proportion to increasing $[MoO_3]$. This change further indicates an increase in the order of the crystalline structure and a reduction in internal stress with $[MoO_3]$.

This result is true except in the case of CNG2.5, which displays the highest fwhm for all powellite $[MoO_4]^{2-}$ modes and also exhibits a larger amorphous contribution detectable

Figure 10. EPR spectra of pristine, 0.77 GGy, and 1.34 GGy β-irradiated samples with 1.75 mol % MoO_3.

through several broad bands before and after irradiation. In Figure 8 we can see not only a relatively higher proportion of broad bands ~500, ~1075, and ~1150 cm^{-1} associated with the silica network but also a strong band at ~910 cm^{-1}. This band is associated with symmetric stretching vibrations of $[MoO_4]^{2-}$ tetrahedral units located in amorphous systems.[39] This result further alludes to a unique composition that results in an increased solubility of molybdenum at 2.5 mol % MoO_3 and a lower crystal quality, which could also account for the irregular CS pattern observed with dose. CNG1.75 also exhibits amorphous bands, but as Figure 8 indicates, they are more prominent in CNG2.5.

In fully amorphous CNO (Figure 9) there are several broad bands at ~450−520 cm^{-1} (Si−O−Si bending),[45,46] ~633 cm^{-1} (Si−O−B vibrations in danburite-like B_2O_7−Si_2O groups[42,46]), ~1445 cm^{-1} (B−O$^-$ bond elongation in metaborate chains and rings[46]), and Si−O stretching vibration modes for Q^n entities that represent SiO_4 units with n bridging oxygen between 845−1256 cm^{-1} (Figure 9). The effects of adding 1 mol % MoO_3 to a soda lime borosilicate glass can be observed in Figure 9. There are three broad bands at ~330, ~870, and ~910 cm^{-1} in CNG1 that describe the order of molybdenum entities in an amorphous phase. Though CNG1 does not show definitive sharp crystal peaks, the broad bands at ~330 and ~870 cm^{-1} are around $[MoO_4]^{2-}$ tetrahedron modes (Figure 8), and the band at ~910 cm^{-1} is related to symmetric stretching as previously mentioned. This indicates that, although dispersed in the borosilicate matrix, molybdenum is still tetrahedrally coordinated with oxygen and exhibits some general order with the Ca^{2+} charge balancers in the vicinity. This result supports the theory that molybdenum, which does not crystallize, remains trapped in an amorphous form of $Ca_x[MoO_4]_y$ in a soda lime borosilicate matrix.[10,47]

While changes to the amorphous phase in GCs are very small as a function of composition, the inclusion of Mo and a Gd dopant in CNG1, CNG1.75, and CNG2.5 is observed to increase the ratios of Q^3 species relative to the broad Si−O−Si bending band, as compared to CNO.

3.32. Irradiated Samples. Modifications to all three Raman parameters are observed in all GCs following irradiation. This suggests a reduction in the crystal quality and a change in lattice parameters. Despite these modifications, the molybdenum tetrahedron retains most of its rigidity, hence why all seven vibrational modes can still be distinctly seen following irradiation (see Figure 8). CN10 and CNG7 have the highest crystalline content, which is why all peaks in the Raman spectra are associated with the powellite phase. Following irradiation most of the peaks experience an increase in the fwhm with dose. Peak broadening is observed to occur in parallel to nonlinear changes in peak area as a function of dose. In CNG7, the peak area of $\nu_2(A_g+B_g)$, $\nu_4(E_g)$, and $\nu_4(B_g)$, normalized to the breathing mode $\nu_1(A_g)$, all increase at a dose of 1.34 GGy relative to samples irradiated to 0.77 GGy. In contrast, the area of these peaks decreased relative to pristine conditions. These observations indicate an increase in the population of certain bending vibrations that are also becoming less ordered or distorted. Or it could signify some preferred orientation within the crystal phase.

There is also a nonlinear effect on peak area with respect to dose in CNG2.5. At 0.77 GGy, the area of $\nu_1(A_g)$ and $\nu_2(A_g+B_g)$ nominally increases, before decreasing below pristine conditions at 1.34 GGy, whereas all other peak areas decrease with dose. Despite the nonlinear changes in peak area with dose, both $\nu_1(A_g)$ and $\nu_2(A_g+B_g)$ peaks exhibit broadening with irradiation, as was previously mentioned to occur in CNG7. The vibrational mode $\nu_1(A_g)$ represents symmetrical stretching vibrations in the molybdate chain, inferring that at 0.77 GGy there is greater order in the unpolymerized cation-rich regions of CNG2.5.

In addition to changes in peak area and width, changes to peak position are also relevant to determine structural modifications. A 0.5−2.0 cm^{-1} shift to lower wavenumbers at 0.77 GGy in CNG7 aligns with a crystallite growth, whereas a shift to higher wavenumbers in CNG2.5 is consistent with a reduction in CS.[41] The opposite trend is observed when the CS of CNG7 decreases at 1.34 GGy and increases for CNG2.5 (see

Supporting Information). However, these peak shifts were not uniform across all modes. In CNG7 peak shifts of ~0.5 cm^{-1} to lower wavenumbers were observed for most peaks save $\nu_4(B_g)$ and $\nu_3(B_g)$, where an ~0.5 cm^{-1} shift to a higher wavenumber was recorded. In a similar manner the peak shift of $\nu_3(E_g)$ in CNG2.5 continuously moved to higher wavenumbers, despite all the other peaks shifting back to lower wavenumber at 1.34 GGy. These nonlinear changes could indicate defects near crystal centers that create anisotropic internal stress and subsequently nonuniform distortions in Mo–O bonds. Or it could be indicative of some preferred orientation.

The Raman spectra of fully amorphous samples do not exhibit great structural modifications following irradiation. However, the broad band in CNG1 around ~870 cm^{-1} analogous to $\nu_1(A_g)$ experiences a shift to higher wavenumbers following irradiation, as well as a nonlinear change in peak area with a maxima at 0.77 GGy. There is also notable broadening of the peak at ~910 cm^{-1}. Additionally, a very small modification in the polymerization index of silica is also present. Before and after irradiation Q^3 (~1075 cm^{-1}) is the most populous Q^n species in CNG1, but both Q^n and the Si–O–Si broad bands decrease with dose.

In the amorphous sample without molybdenum (CNO) only minor changes in the Raman spectra are similarly observed. The primary observation being a shift of 3.0–8.0 cm^{-1} to higher wavenumbers of both the broad band ~500 cm^{-1} and the Q^n modes, which similarly decreases in intensity with dose in most cases. These modifications in silica polymerization are all small, indicating a fairly stable amorphous systems following irradiation.

For GCs that exhibit both amorphous peaks and crystal peaks, such as those with MoO$_3$ in the range of 1.75–2.5 mol %, irradiation initially causes a minor decrease in Q^3/Q^4 for CNG2.5 and an increase for CNG1.75. For higher doses the population of Q^4 is lower at 1.34 GGy than at 0.77 GGy, which is speculated to be a result of defect creation.

3.4. Electronic Defect Structure. Prior to irradiation most samples are EPR-silent, except those doped with gadolinium. In samples with a dopant, EPR analysis reveals the well-known U spectrum ($g \approx 1.0, 2.0, 2.8$) for Gd^{3+} ions with a spin $S = 7/2$ occupying low-symmetry sites.[48] These lines are representative of Gd^{3+} acting as a network modifier (n.m.), while the band at $g \approx 4.8$ is indicative of Gd^{3+} acting as a network former (n.f.)[43] (see Figure 10). A large broad band with a width of 0.6 T is also observed in all samples with Gd and is indicative of superparamagnetic clustering of Gd$_2$O$_3$. The presence of a dopant also sparks a small reduction of Mo^{6+}, which is found to increase with the concentration of MoO$_3$.

After irradiation silicon peroxy radicals ($\equiv$Si–O–O),[49] E' centers ($\equiv$Si$^-$),[50] HC$_1$ centers ($\equiv$Si–O·Na$^+$),[51,52] and boron oxygen hole centers (BOHC) ($\equiv$B–O)[53] were detected empirically in NaBSi, CNO, and CN10 (see Figure 11) as per previous studies. The following assignments for g-tensors were prescribed: E' ($g \approx 2$), BOHC ($g \approx 2.002, 2.013, 2.043$), HC$_1$ ($g \approx 2.002, 2.008, 2.022$), and HC$_2$ ($g \approx 2.001, 2.010, 2.026$) associated with various charge balancers, and Oxy defects ($g \approx 2.003, 2.011, 2.036$). In addition to hole centers in the borosilicate matrix, CN10 also exhibited a reduction of Mo^{6+} at $g \approx 1.911$. All of these compositions had no defects prior to irradiation.

The EPR spectrum in Figure 11 illustrates the compositional effect on the defect structure for this given system. A general broadening of the hyperfine splitting was noted to occur when
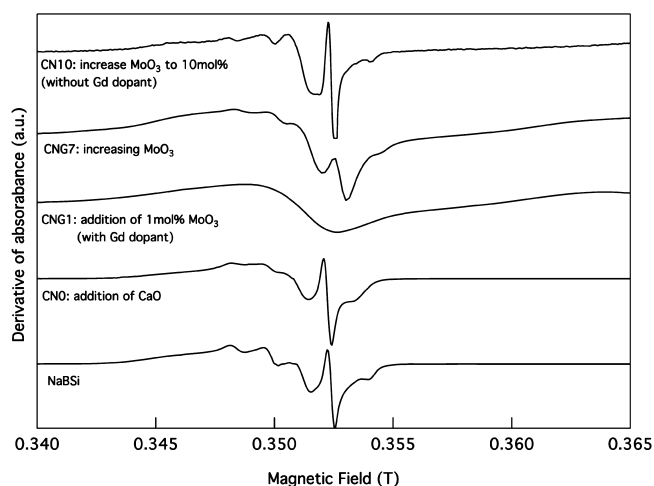
Figure 11. Compositional effects on hyperfine structure of defects induced by 1.34 GGy β-irradiation in EPR spectra. In ascending order: NaBSi; CNO (observed line broadening); CNG1 (observed defect dampening and further broadening); CNG7 (reappearance of hyperfine structure with Gd incorporation into powellite); and CN10.

CaO was included into a sodium borosilicate matrix, but this broadening does not affect the nature of defects formed. Resolution subsequently increased when calcium was taken out of the borosilicate network and incorporated into the crystal phase, as seen in CN10. The presence of a resolved hyperfine structure in CN10, as compared to all other GCs with Gd doping, alludes to the defect dampening effect small amounts of rare-earths can have on the defect structure of the glassy phase[48] in Mo-rich GCs. Several EPR features of the amorphous phase are assigned to compositional responses to irradiation, but dose also altered the defect structure. The relative proportion of E' was found to increase when the dose doubled to 1.34 from 0.77 GGy in all specimens with a resolved hyperfine structure (see Supporting Information).

EPR spectra of all GCs also reveal a strong reduction of Mo^{6+} to Mo^{5+} with the growth of a sharp band at $g \approx 1.911$ in Figure 12, which represents Mo^{5+} diluted in the glassy structure. Mo^{6+} is diamagnetic and hence EPR inactive, so changes in oxidation are easily observed. The reduction of molybdenum induced by
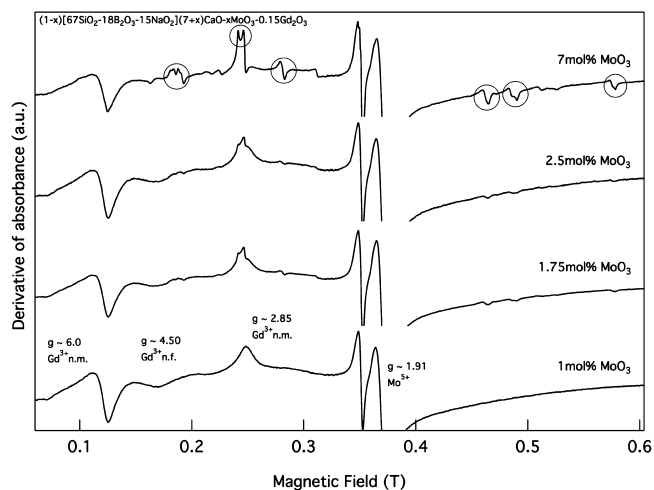
Figure 12. Influence of increasing MoO$_3$ on EPR spectra of 1.34 GGy β-irradiated GCs doped with 0.15 mol % Gd$_2$O$_3$.

irradiation increases with the initial concentration of MoO_3, as illustrated in Figure 12, as well as with dose (Figure 10). The broadening of this single band with irradiation is a result of Mo^{5+} clustering, where dipole–dipole interactions and exchange of coupled Mo^{5+} ions leads to a superposition of the unresolved hyperfine structure.[48,54] An E′ center around $g \approx 2.0$ is also observed in all samples, with or without molybdenum, following irradiation. This defect increases proportionally with dose but at a slower rate than Mo^{6+} reduction. Simultaneous to an increase in the reduction of Mo^{6+} with increasing $[MoO_3]$, we also observe an increase in gadolinium incorporation into the powellite structure, which appeared to increase with dose. Circles on the EPR spectra for CNG7 in Figure 12 indicate Gd^{3+} inclusion bands into the crystalline phase, which can also be seen emerging at lower MoO_3 concentrations. As the amount of Gd^{3+} in powellite increased with dose, the hyperfine structure reappeared for $[MoO_3] > 1$ mol % (tensor visible ~0.35 T).

The relative proportion of gadolinium clustering is observed to decrease with dose in all GCs, which could be correlated to changes in magnetic cluster properties, as the concentration of other defects increases. Or it could be associated with a change in the role and site of Gd^{3+} ions with dose.

4. DISCUSSION

4.1. Compositional Effects on Phase Separation. *4.11. CaMoO₄ Formation during Synthesis.* In general phase separation was proportional to $[MoO_3]$, with two groups of CS (~50 and ~140 nm) and PS (~200−300 and ~600−1000 nm) observed. The composition used in this study facilitated an excess of calcium in Mo-rich regions and had a high-enough concentration of B_2O_3 to ensure that most Na ions were unavailable for molybdate formation. The spherical and unconnected nature of the CaMo-rich particles and distribution within the amorphous matrix indicates a nucleation and growth process initiated by liquid–liquid phase separation.[55] The first stage of separation involves the migration of $[MoO_4]^{2-}$ entities to unpolymerized regions of the glassy network, followed by crystallization of $CaMoO_4$ inside separated phases during cooling.[8,12]

The $CaMoO_4$ CS precipitated on the nanometer scale align with studies based on similar base glasses with a high molybdenum content.[39,40] All of the crystallites take the form of scheelite-type powellite, the tetragonal structure of which is depicted in Figure 13. The lattice parameters observed in this study are initially higher than that of $CaMoO_4$ monocrystals (a = 5.222 Å and c = 11.425 Å[56]), which have been similarly observed to result following a sintering fabrication method.[12,57] Rapidly quenching the system is predicted to cause a contraction of the glassy matrix that creates tensile stress on the $CaMoO_4$ particles. This subsequently does not allow for a full relaxation of $CaMoO_4$ crystals to reach its equilibrium state at room temperature. Thus, creating the discrepancy observed between the cell parameters of crystals embedded in a glass as compared to monocrystals.

Furthermore, we observe that the stress along the c axis is initially greater than that of the a axis. The range of values observed for the a cell parameter between 5.226−5.229 Å are associated with those following heat treatments at 25−100 °C,[58] whereas the range observed for the c cell parameter between 11.455 and 11.460 Å are associated with thermal treatment between 100 and 200 °C.[58] This result indicates that quenching initially caused rigidity primarily in the stacking of
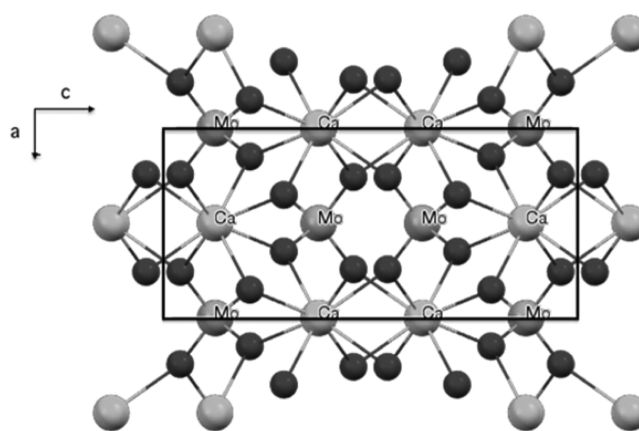
Figure 13. Unit cell of powellite ($CaMoO_4$) as determined by Hazen et al.[56] depicted in Mercury.[60,61]

Ca polyhedra over Mo tetrahedra. This effect is most likely due to temperature effects on sterics between the Mo anion and charge balancers.

Phase separation and crystallization in GCs is significantly affected by both the initial composition and synthesis conditions. In this study, the degree of $CaMoO_4$ phase separation determined by microscopy appears proportional to MoO_3, with the exception of CNG2.5. An increase in $[MoO_3]$ is therefore correlated to phase separation during synthesis. In fact, it has been observed to increase of the immiscibility temperature by ~18 °C per mol of MoO_3,[20] thereby affecting both the phase separation (T_{PS}) and crystallization temperature (T_C). Magnin et al. observed an ~50 °C increase in T_{PS} and ~40 °C increase in T_C of $CaMoO_4$ following an 0.5 mol % increase in MoO_3 from an initial concentration of 2 mol %.[12] For 7 mol % MoO_3 it is estimated that the liquid−liquid T_{PS} increases from ~980 °C at 2 mol % MoO_3 to ~1200−1300 °C,[59] which would thus result in larger areas of separated phases. Correspondingly T_C would increase from ~900 °C at 2 mol % MoO_3 to ~1100 °C.[59] Hence we can assume that the largest PS observed for $MoO_3 \geq 7$ mol % is a result of an increased T_{PS}. Meanwhile the smallest cell parameters are observed at this $[MoO_3]$ as a result of time above the glass transition temperature ($T_C \gg T_g$).

An anomaly occurs when the concentration of MoO_3 is 2.5 mol %, and electron imaging reveals the smallest PS for the series. Moreover, EDS quantitative analysis indicates an excess of calcium near Mo centers, concurrent to a higher concentration of molybdenum in the amorphous network as supported by the Raman spectral mode ~910 cm^{-1}. These findings would indicate a lower T_C as compared to all other GCs. They further suggest a significant fraction of molybdenum dissolved in the matrix of CNG2.5 and that these deposits are in Ca-rich amorphous regions. We can therefore predict that an initial phase separation of Mo−Ca-rich regions occurs, even if crystallization is delayed.

An increased peak broadening of XRD spectra has been previously recorded to occur at 2.5 mol % MoO_3 as compared to other compositions in the range of 1.5−4.5 mol %.[40] In this case, it was proposed that a higher concentration of Gd_2O_3 (1 mol %) increased Mo solubility. As the $[Gd_2O_3]$ is lower in this study, there must be another explanation. Despite a uniform synthesis technique, CNG2.5 appears closer to a metastable equilibrium following melt quenching. This initial condition may encourage rigidity in the crystal system enforced by the

surrounding matrix, thus delaying any CS modifications following irradiation. Alternatively, it could indicate a unique composition that reduces the phase separation and crystallization temperature, by forming a eutectic composition with respect to molybdenum and a borosilicate. Further investigation is required to elucidate this.

The Raman bands can be another metric of phase separation. In an amorphous system, such as CNG1, the band representing Mo−O bond elongation in tetrahedral $[MoO_4]^{2-}$ chains is ~910 cm^{-1}. As partial crystallization commences this band will shift to lower wavenumbers as it approaches perfect symmetry within the Mo tetrahedra.[12,62] Indeed we see that this peak is ~908 cm^{-1} in CNG2.5 and ~905 cm^{-1} in CNG1.75, which supports the theory of crystallization from a Mo−Ca-rich vitreous phase of similar composition to CaMoO$_4$. It further indicates that the crystallization tendency is lower in CNG2.5 than in other GCs.

4.12. Effects of Gadolinium Doping. Gadolinium may be found in the glassy or crystal phase depending on the composition and degree of crystallization. An incorporation of Gd^{3+} ions into the powellite structure appears at higher $[MoO_3]$, concurrent to a transition of Gd^{3+} ions out of the matrix. EPR analysis reveals that incorporation occurs alongside a reduction in paramagnetic clustering, as seen in the spectra for CNG7 (Figure 12). The presence of Gd additionally caused an initial production of Mo^{5+} following GC synthesis (see Figure 10) that was not observed in nondoped CN10. A similar observation was noted to occur in CaWO$_4$ when neodymium was introduced as a dopant,[63] though it is still unclear why this may occur. It is predicted that the presence of Gd^{3+} ions in the depolymerized region internally affected redox conditions.

Trace levels of Gd$_2$O$_3$ appear to aid in the early nucleation of CaMoO$_4$ during synthesis. This effect is based on the relative CS values found in CNG7 and CN10 that were prepared using the same synthesis method and cooling rate. Platinoid heterogeneities in nuclear waste glasses have been observed to enhance crystal nucleation by reducing the liquid-crystal interfacial energy and therefore the thermodynamic barrier to crystallization by roughly 3 orders of magnitude.[64] As both the original CS and the rate of change induced by irradiation are both larger in CNG7 than they are in CN10, we assume that gadolinium inclusion affects both nucleation and growth kinetics, thus outlining the effects of trace incorporation.

4.2. Irradiation Effects. 4.21. Modifications to Borosilicate Glass Network. The soda lime borosilicate matrix investigated in this study does not experience significant structural modifications following β-irradiation. Nearly all the $[MoO_4]^{2-}$ tetrahedra were charge-balanced with Ca^{2+} ions whether in a crystalline or amorphous phase. Additionally, no glass-in-glass phase separation, which has been known to occur following β-irradiation into alkali boron-rich and silica-rich regions,[1,34] was detected at these doses, dose rates, and compositions.

The evolution of silica polymerization (Q^n species) with dose appeared dependent on the initial composition, as different trends were observed for different samples. Previous studies of soda lime borosilicates have observed an increase in polymerization following irradiation,[33,65] though significant changes were not detected in this study. We can predict that modifications were limited by irradiation-induced defects in this specific compositional series.

These results therefore indicate a general stability against phase separation in both the amorphous system and in precipitating out a crystalline phase in an initially amorphous system. This latter observation is based on CNG1 remaining fully amorphous following irradiation. Furthermore, no local fractures near the crystal−glass interface or global cracking were observed in GCs by SEM. That is not to say that they do not exist, but that if they do, they will be few in number.

4.22. Gadolinium Incorporation by Irradiation. Gadolinium doping causes a broadening of the hyperfine structure in EPR spectra. This result indicates that, while Gd^{3+} ions are in the glassy matrix, they aid in either dampening BOHC, HC$_1$, and Oxy defects or that dipole−dipole interactions arising from Gd^{3+} ions in the vicinity of other defects causes significant broadening and thus resolution distortion. Given the low concentration of Gd, the former explanation is more likely.

At higher $[MoO_3]$ an incorporation of Gd^{3+} ions into the powellite structure appears, indicating a transition of Gd^{3+} ions out of the matrix. EPR analysis reveals that this occurs alongside a reduction in paramagnetic clustering and an emergence of the hyperfine structure as seen in the EPR spectra for CNG7 (Figure 12).

Incorporation of gadolinium into powellite seems initiated by composition and exacerbated by irradiation. This phenomena has been previously observed to occur when $[MoO_3] \geq 5$ mol % in soda lime borosilicates through a combined Na−Gd substitution of Ca^{2+} ions.[40] The mechanism of substitution in this study was not clear, as Gd$_{0.5}$Na$_{0.5}$CaMoO$_4$ crystalline markers were not detected on XRD spectra. Refinement of the calcium site occupancy in CaMoO$_4$ has been previously used to detect substitution of Ca cations with other charge balancers, particularly in the case of rare-earth substitution where the covalent size of elements differs substantially.[43,66] In this study, we detect no such substitution following refinement. While XRD was not able to detect incorporation, Raman results showing a nonlinear alteration to peak area and peak shifts of $[MoO_4]^2$ vibrational modes could be a result of Gd substitution. Conversion of the octahedrally coordinated site from S_4 to C_{2v} point group induced by Gd substitution into the powellite structure[67] following irradiation could be responsible for the observed nonlinear shifts. It could also account for the nonuniform peak area growth of ν_4 bands, which represent deformation modes of terminal units.

Whereas the presence of Gd may affect Mo reduction and solubility as previously mentioned, it does not have a direct effect on the type of other defects induced in the glassy matrix. The defect structure found in all the compositions without Gd by EPR was similar to those detected in GCs with Gd doping when Gd^{3+} was incorporated into powellite (Figure 11). These observations indicate that the behavioral pattern of defect creation in a soda lime borosilicate matrix can be easily predicted, independent of dopants and CaMoO$_4$ crystallization.

4.23. Radiation Stability of CaMoO$_4$. This study confirms resistance of CaMoO$_4$ to β-irradiation at the anticipated dose following 1000 years of encapsulation when embedded in a borosilicate glass matrix. Marginal losses in crystal quality and isotropic distortions in the CaMoO$_4$ structure were presumed to be a result of defect creation resulting from irradiation. Most importantly these modifications do not end in amorphization. Furthermore, Gd^{3+} incorporation into the powellite phase detected by EPR spectroscopy is not visible by XRD, indicating that incorporation is only at trace levels. It could also indicate that lattice distortions induced by substitution on this scale are minor and do not significantly alter the crystallography of the bulk and therefore the physical properties. This is an important

consideration for active waste glasses containing minor actinides.

Isotropic changes in the crystal structure are reflected in the CS patterns deduced from refinement of XRD patterns. A similar pattern in cell parameters is observed for all samples with $CaMoO_4$ crystals, but variations in CS suggest radiation effects acting through multiple channels. Radiation-induced relaxation and diffusion replicating thermal processes, as well as the initial composition and defect distribution, all have roles to play in CS determination following irradiation.

Let us first consider an analogous temperature-based approach. The reduction of cell parameters observed in CN10, CNG7, and CNG1.75 by XRD could contribute to relaxation of the tensile stress induced during synthesis. Stress reduction would correspondingly result in an increase of CS, as these two parameters have opposing trends on diffraction peak broadening. The added energy associated with electron irradiation could enable local relaxation causing a reduction of the unit cell parameters toward the equilibrium state of $CaMoO_4$ monocrystals. This is empirically observed to occur primarily along the c-axis at 0.77 GGy, presumably because the initial stress induced during synthesis was higher in this direction. The thermal expansion of powellite has been seen to exhibit anisotropic behavior with the coefficient of thermal expansion along the c-axis being almost double that along the a-axis.[58,68] Temperature-induced expansion lay primarily along Ca–O bonds in CaO_8 polyhedra, where the MoO_4 tetrahedra are characteristically rigid with limited expansion. While the cell parameters are observed to decrease in this study, β-irradiation-induced changes to powellite correspondingly have a higher stress along the c-axis. This parallel further supports the theory that the c axis has a greater susceptibility to modifications during synthesis and following irradiation. However, in two of the samples we also saw a reduction in a at this dose, indicating that the initial internal stresses vary with composition.

This hypothesis of directional changes is supported by the fact that all $[MoO_4]^{2-}$ Raman modes in all GCs are present following irradiation. It indicates that Mo tetrahedral units are rigid and that modifications observed by XRD and SEM are likely due to alteration between the Mo tetrahedra and the charge-balancing Ca^{2+} cations. This would result in alterations to the c axis, as XRD refinement indicates. This is not to say that defects do not alter the Mo–O bond in the Mo tetrahedra, but that β-irradiation has a greater initial effect on the Ca⋯Mo bond distance, as the bond affinity is lower. The visualization in Figure 13 illustrates the Ca polyhedra stacking along the c axis and the Mo tetrahedra stacking along a axis, which can help explain this theory. This is why thermal treatments and pressure-induced compression[56] likewise effects the Ca polyhedra preferentially. Raman shifts similar to some of those observed in this study have also been previously recorded to occur as a result of compression along the c-axis.[68,69] Moreover, quantitative analysis by EDS further supports this theory with observed migration of Ca atoms away from crystal centers.

In terms of the CS trend observed for these samples, the growth and then reduction of CS could be due to several reasons. Either growth is due to precipitation of $CaMoO_4$ on existing crystals, or there is a reduction of mosaicity following irradiation. If the latter, we would expect to see an increase in the coherency length, which would be reflected in the CS estimates (Table 2). Using this interpretation, a reduction in CS could be associated with an increase in disorder within the crystalline phase. Therefore, an increase in order would have the opposite response. If CS growth is dependent on conglomeration, we could be seeing the effects of diffusion that are kinetically driven by inputted energy or by defects that create migration channels following irradiation. These considerations would account for the CS growth seen at 0.77 GGy, as well as the reduction in smaller PS by SEM, but not the reduction observed at 1.34 GGy. For this, we need to further consider the defect structure.

EPR spectra reveal a range of defects that increases with dose. At 0.77 GGy a destabilization stage is expected, when electronic defects are first introduced into the system. These localized defects created in the matrix may be aiding in any diffusion or relaxation processes, which would enable CS growth. As dose increases to 1.34 GGy it is predicted that internal microstrain created by defect accumulation is the driving force in XRD peak broadening. As the data collected in this study were only suitable for a single parameter fit, changes in CS must be attributed to both size and microstrain. Williamson–Hall plots were constructed on the most crystalline sample CN10 to confirm this theory (Supporting Information).

Speculation must be made on the defects that could be inducing this strain. One theory is that vacancy clusters cause a compression of crystallites. In literature, irradiation-induced reduction of glass has been hypothesized to initiate the removal of NBOs in a borosilicate network and create neutral Ca or Na atoms.[27,49] The atoms created by this process will be free to migrate around the glassy network and will likely cluster in vacancies or become trapped near hole centers.[53] Indeed the clustering of alkali ions and subsequent hole trapping is a recorded effect of β-irradiation, which is known to also induce cationic mobility.[28,30] The vacancies described above, which could act as neutral atom sinks, are themselves a result of increasing dose, where their creation can be initiated from hole centers (E′, BOHC, HC_1, and HC_2). Furthermore, an observed broadening of defects in EPR spectra with dose can be attributed to dipole–dipole interactions, which alludes to defects structurally occurring in proximity to each other. This would thus enable a precursor environment for vacancies to form. If vacancy clusters are in the vicinity of Mo-rich regions, it can cause a compressive effect on the crystal clusters. This effect would be further exacerbated by the presence of neutral atoms, as this would increase the exerted vacancy pressure. An assumption is being made in that the defects detected by EPR are indicative of those consumed by structural changes in powellite, as observed through other lower-sensitivity analytical techniques. This assumption enables a correlation to be drawn between dilute defects observed by EPR and those describing long-range order. Alternatively, we could be seeing an accumulation of defects within the crystals themselves, which would cause a reduction in the coherency length and therefore a reduction in CS.

4.24. Proposed Theory for CS Alteration of $CaMoO_4$. The model proposed to account for changes in CS observed in this study is based on empirical evidence. It is presumed to be dependent on the impact of two parameters, which have different relationships with respect to time. They are (A) radiation-induced relaxation and diffusion that replicate thermal processes and (B) electronic defect accumulation, which presents itself as increased internal microstrain. At lower doses, relaxation from added energy and point defects, as well as diffusion-based growth, are the prevailing forces in

determining the growth of CS. It is predicted that a kinetic barrier to diffusion of ions in the glassy matrix exists and that CS growth reaches saturation quickly. This trend is observed for Orlhac's investigations, where CS growth showed a square root of time at temperature dependence, indicative of a kinetic process limited by diffusion in the glass network.[64] In an analogous form, accumulated dose at 0.77 GGy could represent a growth plateau in most of the samples, and subsequent modifications are primarily due to defect accumulation and compression prevalent at higher doses.

Parameter A in the proposed model is predicted to follow a logarithmic relationship with dose, displaying effects early. This is based on the assumption that thermal-like effects follow Arrhenius laws and that radiation exceeds E_a at 0.77 GGy. In comparison, parameter B follows a sigmoidal function displaying effects later for a maximum of 1.34 GGy. While defect creation may grow linearly with dose, it is presumed that there exists a barrier to defect clustering and vacancy creation. Though a sigmoidal function is assumed for this simplified model using data from only two doses, defect accumulation may very well follow an damped oscillating pattern for doses greater than 1.34 GGy. Defects cannot indefinitely exist in any structure due to the strain that they exert. When they can no longer be supported, they could be alleviated through dislocations, thus releasing pressure on the crystal system as proposed by Jagieleski et al[70] in his multistep model for damage accumulation. This effect would present itself as an increase in CS. At a constant fluence, defects would again begin to increase, causing an increase in strain and a reduction in CS again. However, structural modifications induced by radiation damage are not fully reversible, and an overall saturation effect is expected at very high doses, hence a predicted damped relationship.

Parameter A is therefore predicted to cause growth, and parameter B causes a reduction, by way of increased strain. At 1.34 GGy the effects of diffusion-based growth are assumed to be limited by the structural changes induced by clustered point defects; hence, the effects of parameter A are less significant.

CS changes in CN10, CNG7, and CNG1.75 are presumed to follow this model, as all three samples exhibit a similar CS pattern with respect to dose, where minor variations can be attributed to Gd inclusion in doped samples. In contrast, CNG2.5 displays an opposing trend in CS. Despite this variation, a reduction of cell parameters, with the alteration predominantly along the c-axis, is similarly observed. This indicates that relaxation alone cannot account for changes in CS. This observation is simultaneous to an increase in $[Mo^{5+}]$, which was also observed in other GCs. This could indicate that the nature of defects formed in not controlling defect accumulation. Therefore, changes to the glassy matrix and the initial phase separation must account for the CS variation in this sample. An initial rigidity in the distribution of ion channels and an increased solubility of Mo during synthesis is theorized to account for the delayed diffusion to crystal centers and therefore CS growth, thus shifting the weighting of parameter A so that parameter B (defect-induced alteration within the crystal structure) becomes more significant at low doses.

5. CONCLUSIONS

Simplified glass ceramics were successfully synthesized to promote the crystallization of $CaMoO_4$ and prevent the speciation of Na_2MoO_4 for up to 10 mol % MoO_3 by introducing MoO_3 in a 1:1 ratio to CaO. The morphology and distribution of crystallites indicated a nucleation and growth process, where the degree of phase separation was proportional to $[MoO_3]$ and molybdenum had a similar structure in both the amorphous and crystalline phases.

Trace levels of gadolinium ions served as both a nucleating agent and as an electronic defect dampener when diluted in the amorphous phase. Minor incorporation of Gd^{3+} into $CaMoO_4$ observed by EPR indicates that at higher concentrations there may be significant inclusion of minor actinides in more complex systems, especially as this incorporation increased with dose.

In $CaMoO_4$ crystals, a nonlinear CS growth is observed with dose and composition. A two-stage process with various weighting factors associated with radiation-induced relaxation and diffusion-replicating thermal processes and defect accumulation is proposed to account for the CS pattern of $\Delta_{CS} = \pm 15-57$ nm at 0.77 GGy, which returns to almost pristine conditions at 1.34 GGy. Lattice relaxation and kinetic diffusion of cationic species are used to explain CS growth, while defect accumulation that created free volume and subsequently internal microstrain explains CS reduction. The prevalence of one effect over the other is dependent on the initial fabrication quench rate, the composition, and the overall concentration of electronic defects in the structure. Though a nonlinear CS pattern with respect to dose was observed, a reduction in cell parameters with prevalence along the c-axis occurred in all GCs approaching $CaMoO_4$ monocrystal parameters.

Overall, we can conclude that the glassy network behaved as expected and did not elicit precipitation following irradiation and that $CaMoO_4$ crystals showed resistance to amorphization for particles greater than 150 nm in size. Radiation does not increase the propagation of crystalline precipitation, but it does aid in growth by redistribution at some doses. We cannot definitively comment on this original hypothesis due to the nonlinearity of CS with dose and the limited data set.

■ ASSOCIATED CONTENT

ⓈSupporting Information

The Supporting Information is available free of charge on the ACS Publications website at DOI: 10.1021/acs.inorg-chem.6b02657.

> Additional XRD spectra for powdered pristine samples and Rietveld refinement of size and microstrain for CN10; SEM images of pristine amorphous samples, EDS of GC prior to irradiation and expansion on sampling technique; table of Raman spectra peak fitting of both the crystalline and amorphous phases, as well as additional trends; additional EPR spectra of irradiated NaBSi and CN10 (PDF)
>
> Williamson & Hall plots for CN10 with Miller indices in xlsx format (zip−Macintosh) (ZIP)

■ AUTHOR INFORMATION

Corresponding Author

*E-mail: kp391@cam.ac.uk.

ORCID ⓘ

Karishma B. Patel: 0000-0001-5787-2422

Present Address

△Laboratoire des Solides Irradiés, CNRS-UMR 7642, CEA-DRF-IRAMIS, Ecole Polytechnique, Université Paris-Saclay, Palaiseau Cedex, 91120, France

Author Contributions

‖The manuscript was written through various contributions of all authors, and all authors have given approval to the final version of the manuscript. These authors contributed equally. K.P. wrote manuscript and performed bulk of synthesis and analysis, of which I.F. supervised as principal investigator. S.S. and S.P. aided in discussion of results as part of collaboration between the CEA and the Univ. of Cambridge. B.B. ran irradiation facility and aided in the collection and interpretation of EPR results. G.L. made significant contributions to analysis of XRD data, and S.F. maintained and calibrated Raman equipment.

Notes

The authors declare no competing financial interest.

◼ REFERENCES

(1) Lee, W. E.; Ojovan, M. I.; Stennett, M. C.; Hyatt, N. C. Immobilisation of Radioactive Waste in Glasses, Glass Composite Materials and Ceramics. *Adv. Appl. Ceram.* **2006**, *105*, 3−12.

(2) Peuget, S.; Cachia, J.-N.; Jégou, C.; Deschanels, X.; Roudil, D.; Broudic, V.; Delaye, J. M.; Bart, J.-M. Irradiation Stability of R7T7-Type Borosilicate Glass. *J. Nucl. Mater.* **2006**, *354*, 1−13.

(3) Frugier, P.; Martin, C.; Ribet, I.; Advocat, T.; Gin, S. The Effect of Composition on the Leaching of Three Nuclear Waste Glasses: R7T7, AVM and VRZ. *J. Nucl. Mater.* **2005**, *346*, 194−207.

(4) Gras, J. M.; Quang, R. D.; Masson, H.; Lieven, T.; Ferry, C.; Poinssot, C.; Debes, M.; Delbecq, J. M. Perspectives on the Closed Fuel Cycle - Implications for High-Level Waste Matrices. *J. Nucl. Mater.* **2007**, *362*, 383−394.

(5) Magnin, M.; Schuller, S.; Mercier, C.; Trébosc, J.; Caurant, D.; Majérus, O.; Angéli, F.; Charpentier, T. Modification of Molybdenum Structural Environment in Borosilicate Glasses with Increasing Content of Boron and Calcium Oxide by ⁹⁵Mo MAS NMR. *J. Am. Ceram. Soc.* **2011**, *94*, 4274−4282.

(6) Dunnett, B. F.; Gribble, N. R.; Short, R.; Turner, E.; Steele, C. J.; Riley, A. D. Vitrification of High Molybdenum Waste. *Glas. Technol. Eur. J. Glas. Sci. Technol. Part A* **2012**, *53*, 166−171.

(7) Chouard, N.; Caurant, D.; Majérus, O.; Dussossoy, J. L.; Ledieu, A.; Peuget, S.; Baddour-Hadjean, R.; Pereira-Ramos, J. P. Effect of Neodymium Oxide on the Solubility of MoO₃ in an Aluminoborosilicate Glass. *J. Non-Cryst. Solids* **2011**, *357*, 2752−2762.

(8) Caurant, D.; Majérus, O.; Fadel, E.; Lenoir, M.; Gervais, C.; Pinet, O. Effect of Molybdenum on the Structure and on the Crystallization of SiO₂-Na₂O-CaO-B₂O₃ Glasses. *J. Am. Ceram. Soc.* **2007**, *90*, 774−783.

(9) Short, R. J.; Hand, R. J.; Hyatt, N. C.; Möbus, G. Environment and Oxidation State of Molybdenum in Simulated High Level Nuclear Waste Glass Compositions. *J. Nucl. Mater.* **2005**, *340*, 179−186.

(10) Caurant, D.; Majérus, O.; Fadel, E.; Quintas, A.; Gervais, C.; Charpentier, T.; Neuville, D. Structural Investigations of Borosilicate Glasses Containing MoO₃ by MAS NMR and Raman Spectroscopies. *J. Nucl. Mater.* **2010**, *396*, 94−101.

(11) Calas, G.; Le Grand, M.; Galoisy, L.; Ghaleb, D. Structural Role of Molybdenum in Nuclear Glasses: An EXAFS Study. *J. Nucl. Mater.* **2003**, *322*, 15−20.

(12) Magnin, M. Étude Des Processus de Demixtion et de Cristallisation Au Sein de Liquides Fondus Borosilicatés Riches En Oxyde de Molybdène. Ph.D. Thesis (French), Université Pierre et Marie Curie, 2009.

(13) Nicoleau, E.; Schuller, S.; Angeli, F.; Charpentier, T.; Jollivet, P.; Le Gac, A.; Fournier, M.; Mesbah, A.; Vasconcelos, F. Phase Separation and Crystallization Effects on the Structure and Durability of Molybdenum Borosilicate Glass. *J. Non-Cryst. Solids* **2015**, *427*, 120−133.

(14) Short, R. Phase Separation and Crystallisation in UK HLW Vitrified Products. *Procedia Mater. Sci.* **2014**, *7*, 93−100.

(15) Rose, P. B.; Woodward, D. I.; Ojovan, M. I.; Hyatt, N. C.; Lee, W. E. Crystallisation of a Simulated Borosilicate High-Level Waste Glass Produced on a Full-Scale Vitrification Line. *J. Non-Cryst. Solids* **2011**, *357*, 2989−3001.

(16) Weber, W. J.; Ewing, R. C.; Angell, C. A.; Arnold, G. W.; Delaye, J. M.; Hobbs, L. W.; Price, D. L.; et al. Radiation Effects in Glasses Used for Immobilization of High-Level Waste and Plutonium Disposition. *J. Mater. Res.* **1997**, *12*, 1948−1978.

(17) Crum, J. V.; Riley, B. J.; Turo, L. R.; Tang, M.; Kossoy, A. *Summary Report: Glass-Ceramic Waste Forms for Combined Fission Products*; Technical Report for U.S. Department of Energy, Pacific Northwest National Laboratory, 2011.

(18) Quang, R. D.; Petitjean, V.; Hollebecque, F.; Pinet, O.; Flament, T.; Prod'homme, A. Vitrification of HLW Produced by Uranium/Molybdenum Fuel Reprocessing in COGEMA's Cold Crucible Melter. In *Waste Management Symposium*; ASME 2003 9th International Conference on Radioactive Waste Management and Environmental Remediation; Oxford, England, Sept 21−25, 2003; ASME: New York, **2003**; p 158510.1115/ICEM2003-4594

(19) Schuller, S.; Pinet, O.; Grandjean, A.; Blisson, T. Phase Separation and Crystallization of Borosilicate Glass Enriched in MoO₃, P₂O₅, ZrO₂, CaO. *J. Non-Cryst. Solids* **2008**, *354*, 296−300.

(20) Kawamoto, Y.; Clemens, K.; Tomozawa, M. Effects of MoO3 on Phase Separation of Na₂0-B₂0₃-Si0₂ Glasses. *J. Am. Ceram. Soc.* **1981**, *64*, 292−296.

(21) Magnin, M.; Schuller, S.; Mercier, C.; Trébosc, J.; Caurant, D.; Majérus, O.; Angéli, F.; Charpentier, T. Modification of Molybdenum Structural Environment in Borosilicate Glasses with Increasing Content of Boron and Calcium Oxide by ⁹⁵Mo MAS NMR. *J. Am. Ceram. Soc.* **2011**, *94*, 4274−4282.

(22) Horneber, A.; Camara, B.; Lutze, W. Investigation on the Oxidation State and The Behaviour of Molybdenum in Silicate Glass. *MRS Online Proc. Libr.*; **1981**; Vol. *11*, pp 279−288.10.1557/PROC-11-279

(23) Quintas, a.; Caurant, D.; Majérus, O.; Charpentier, T.; Dussossoy, J. L. Effect of Compositional Variations on Charge Compensation of AlO4 and BO4 Entities and on Crystallization Tendency of a Rare-Earth-Rich Aluminoborosilicate Glass. *Mater. Res. Bull.* **2009**, *44*, 1895−1898.

(24) Ojovan, M. I.; Lee, W. E. *An Introduction to Nuclear Waste Immobilisation*; Elsevier, 2005.

(25) Gutierrez, G.; Peuget, S.; Hinks, J. A.; Greaves, G.; Donnelly, S. E.; Oliviero, E.; Jégou, C. Helium Bubble Formation in Nuclear Glass by in-Situ TEM Ion Implantation. *J. Nucl. Mater.* **2014**, *452*, 565−568.

(26) Delaye, J.-M.; Peuget, S.; Bureau, G.; Calas, G. Molecular Dynamics Simulation of Radiation Damage in Glasses. *J. Non-Cryst. Solids* **2011**, *357*, 2763−2768.

(27) Griscom, D. L. Trapped-Electron Centers in Pure and Doped Glassy Silica: A Review and Synthesis. *J. Non-Cryst. Solids* **2011**, *357*, 1945−1962.

(28) Boizot, B.; Petite, G.; Ghaleb, D.; Calas, G. Radiation Induced Paramagnetic Centres in Nuclear Glasses by EPR Spectroscopy. *Nucl. Instrum. Methods Phys. Res., Sect. B* **1998**, *141*, 580−584.

(29) DeNatale, J. F.; McElfresh, D. K.; Howitt, D. G. Radiation Effects in Nuclear Waste Glasses. *MRS Online Proc. Libr.* **1981**, *6*, 697−702.

(30) Ollier, N.; Champagnon, B.; Boizot, B.; Guyot, Y.; Panczer, G.; Padlyak, B. Influence of External β-Irradiation in Oxide Glasses. *J. Non-Cryst. Solids* **2003**, *323*, 200−206.

(31) Malchukova, E.; Boizot, B. Reduction of Eu^{3+} to Eu^{2+} in Aluminoborosilicate Glasses under Ionizing Radiation. *Mater. Res. Bull.* **2010**, *45*, 1299−1303.

(32) Ollier, N.; Boizot, B.; Reynard, B.; Ghaleb, D.; Petite, G. β Irradiation in Borosilicate Glasses: The Role of the Mixed Alkali Effect. *Nucl. Instrum. Methods Phys. Res., Sect. B* **2004**, *218*, 176−182.

(33) Boizot, B.; Petite, G.; Ghaleb, D.; Calas, G. *J. Non-Cryst. Solids* **2001**, *283*, 179−185.

(34) Sun, K.; Wang, L. M.; Ewing, R. C.; Weber, W. J. Electron Irradiation Induced Phase Separation in a Sodium Borosilicate Glass. *Nucl. Instrum. Methods Phys. Res., Sect. B* **2004**, *218*, 368−374.

(35) Peuget, S.; Delaye, J. M.; Jégou, C. Specific Outcomes of the Research on the Radiation Stability of the French Nuclear Glass towards Alpha Decay Accumulation. *J. Nucl. Mater.* **2014**, *444*, 76−91.

(36) Payzant, E. A. Other Topics. In *Principles and Applications of Powder Diffraction*; Clearfield, A., Reibenspies, J., Bhuvanesh, N., Eds.; John Wiley and Sons, Ltd., 2008; pp 365−380.

(37) Black, D. R.; Windover, D.; Henins, A.; Filliben, J.; Cline, J. P. Certification of Standard Reference Material 660B. *Powder Diffr.* **2011**, *26*, 155−158.

(38) Cheary, R. W.; Coelho, A. a.; Cline, J. P. Fundamental Parameters Line Profile Fitting in Laboratory Diffractometers. *J. Res. Natl. Inst. Stand. Technol.* **2004**, *109*, 1−25.

(39) Chouard, N.; Caurant, D.; Majérus, O.; Dussossoy, J. L.; Klimin, S.; Pytalev, D.; Baddour-Hadjean, R.; Pereira-Ramos, J. P. Effect of MoO_3, Nd_2O_3, and RuO_2 on the Crystallization of Soda−lime Aluminoborosilicate Glasses. *J. Mater. Sci.* **2015**, *50*, 219−241.

(40) Taurines, T.; Boizot, B. Microstructure of Powellite-Rich Glass-Ceramics: A Model System for High Level Waste Immobilization. *J. Am. Ceram. Soc.* **2012**, *95*, 1105−1111.

(41) Wang, X.; Panczer, G.; de Ligny, D.; Motto-Ros, V.; Yu, J.; Dussossoy, J. L.; Peuget, S.; Jóźwik-Biala, I.; Bérerd, N.; Jagielski, J. Irradiated Rare-Earth-Doped Powellite Single Crystal Probed by Confocal Raman Mapping and Transmission Electron Microscopy. *J. Raman Spectrosc.* **2014**, *45*, 383−391.

(42) Frost, R. L.; Bouzaid, J.; Butler, I. S. Raman Spectroscopic Study of the Molybdate Mineral Szenicsite and Com- Pared with Other Paragenetically Related Molybdate Minerals. *Spectrosc. Lett.* **2007**, *40*, 603−614.

(43) Taurines, T.; Neff, D.; Boizot, B. Powellite-Rich Glass-Ceramics: A Spectroscopic Study by EPR and Raman Spectroscopy. *J. Am. Ceram. Soc.* **2013**, *96*, 3001−3007.

(44) Crane, M.; Frost, R. L.; Williams, P. A.; Theo Kloprogge, J. Raman Spectroscopy of the Molybdate Minerals Chillagite (Tung-steinian Wulfenite-I4), Stolzite, Scheelite, Wolframite and Wulfenite. *J. Raman Spectrosc.* **2002**, *33*, 62−66.

(45) Neuville, D. R.; Cormier, L.; Boizot, B.; Flank, A. M. Structure of β-Irradiated Glasses Studied by X-Ray Absorption and Raman Spectroscopies. *J. Non-Cryst. Solids* **2003**, *323*, 207−213.

(46) Bonfils, J. de; Peuget, S.; Panczer, G.; Ligny, D. de; Henry, S.; Noël, P.-Y.; Chenet, A.; Champagnon, B. Effect of Chemical Composition on Borosilicate Glass Behavior under Irradiation. *J. Non-Cryst. Solids* **2010**, *356*, 388−393.

(47) Henry, N.; Deniard, P.; Jobic, S.; Brec, R.; Fillet, C.; Bart, F.; Grandjean, A.; Pinet, O. Heat Treatments versus Microstructure in a Molybdenum-Rich Borosilicate. *J. Non-Cryst. Solids* **2004**, *333*, 199−205.

(48) Malchukova, E.; Boizot, B.; Ghaleb, D.; Petite, G. β-Irradiation Effects in Gd-Doped Borosilicate Glasses Studied by EPR and Raman Spectroscopies. *J. Non-Cryst. Solids* **2006**, *352*, 297−303.

(49) Dutt, D. A.; Higby, P. L.; Griscom, D. L. An Electron Spin Resonance Study of X-Irradiated Calcium Aluminosilicate Glasses. *J. Non-Cryst. Solids* **1991**, *130*, 41−51.

(50) Weeks, R. A. The Many Varieties of E′ Centers: A Review. *J. Non-Cryst. Solids* **1994**, *179*, 1−9.

(51) Griscom, D. L. Electron Spin Resonance Studies of Trapped Hole Centers in Irradiated Alkali Silicate Glasses: A Critical Comment on Current Models for HC1 and HC2. *J. Non-Cryst. Solids* **1984**, *64*, 229−247.

(52) Agnello, S.; Gelardi, F. M.; Boscaino, R.; Cannas, M.; Boizot, B.; Petite, G. Intrinsic Defects Induced by β-Irradiation in Silica. *Nucl. Instrum. Methods Phys. Res., Sect. B* **2002**, *191*, 387−391.

(53) Griscom, D. L. E.S.R. Studies of Radiation Damage and Structure in Oxide Glasses Not Containing Transition Group Ions: A Contemporary Overview with Illustrations from the Alkali Borate System. *J. Non-Cryst. Solids* **1974**, *13*, 251−285.

(54) Toloman, D.; Ciceo-Lucacel, R.; Magdas, D. A.; Regos, A.; Biris, A. R.; Leostean, C.; Ardelean, I. The Modifier/former Role of MoO_3 in Some Calcium-Phosphate Glasses. *J. Alloys Compd.* **2013**, *556*, 67−70.

(55) Cousi, C.; Bart, F.; Base, E. De; Valrhô, C. E. A.; Dtcd, M. D. E. N.; Cedex, B.; Verres, L.; Montpellier, U. De. Phase Separation and Crystallisation Induced by Adding Molybdenum and Phosphorus to a Soda-Lime-Silica Glass. *Glass Technol.* **2004**, *45*, 2003−2005.

(56) Hazen, R. M.; Finger, L. W.; Mariathasan, J. W. E. High-Pressure Crystal Chemistry of Scheelite-Type Tungstates and Molybdates. *J. Phys. Chem. Solids* **1985**, *46*, 253−263.

(57) Mendoza, C. Caracterisation et Comportement Sous Irradiation de Phases Powellites Dopees Terres Rares—Application Au Comportement a Long Terme Des Matrices de Confinement Des Dechets Nuclement. Ph.D. Thesis (French), Universite Claude Bernard Lyon 1: Lyon, France, 2010.

(58) Achary, S. N.; Patwe, S. J.; Mathews, M. D.; Tyagi, A. K. High Temperature Crystal Chemistry and Thermal Expansion of Synthetic Powellite ($CaMoO_4$): A High Temperature X-Ray Diffraction (HT-XRD) Study. *J. Phys. Chem. Solids* **2006**, *67*, 774−781.

(59) Schuller, S.; Pinet, O.; Penelon, B. Liquid-Liquid Phase Separation Process in Borosilicate Liquids Enriched in Molybdenum and Phosphorus Oxides. *J. Am. Ceram. Soc.* **2011**, *94*, 447−454.

(60) Bruno, I. J.; Cole, J. C.; Edgington, P. R.; Kessler, M.; Macrae, C. F.; McCabe, P.; Pearson, J.; Taylor, R. New Software for Searching the Cambridge Structural Database and Visualizing Crystal Structures. *Acta Crystallogr., Sect. B: Struct. Sci.* **2002**, *58*, 389−397.

(61) Macrae, C. F.; Edgington, P. R.; McCabe, P.; Pidcock, E.; Shields, G. P.; Taylor, R.; Towler, M.; Van De Streek, J. Mercury: Visualization and Analysis of Crystal Structures. *J. Appl. Crystallogr.* **2006**, *39*, 453−457.

(62) Hardcastle, F. D.; Wachs, I. E. Determination of Molybdenum-Oxygen Bond Distances and Bond Orders by Raman Spectroscopy. *Solid State Ionics* **1991**, *45*, 201−213.

(63) Azarbayejani, G. H.; Merlo, A. L. Electron Spin Resonance of Mo^{5+} in $CaWO_4$. *Phys. Rev.* **1965**, *137*, A489−490.

(64) Orlhac, X.; Fillet, C.; Phalippou, J. Study of Crystallization Mechanisms in the French Nuclear Waste Glass. In *MRS Online Proc. Libr.*; 1999; Vol. *556*, pp 263−270.10.1557/PROC-556-263

(65) Yang, K. J.; Wang, T. S.; Zhang, G. F.; Peng, H. B.; Chen, L.; Zhang, L. M.; Li, C. X.; Tian, F.; Yuan, W. Study of Irradiation Damage in Borosilicate Glass Induced by He Ions and Electrons. *Nucl. Instrum. Methods Phys. Res., Sect. B* **2013**, *307*, 541−544.

(66) Orlhac, X.; Fillet, C.; Deniard, P.; Dulac, A. M.; Brec, R. Determination of the Crystallized Fractions of a Largely Amorphous Multiphase Material by the Rietveld Method. *J. Appl. Crystallogr.* **2001**, *34*, 114−118.

(67) Schmidt, M.; Heck, S.; Bosbach, D.; Ganschow, S.; Walther, C.; Stumpf, T. Characterization of Powellite-Based Solid Solutions by Site-Selective Time Resolved Laser Fluorescence Spectroscopy. *Dalt. Trans.* **2013**, *42*, 8387.

(68) Christofilos, D.; Kourouklis, G. a.; Ves, S. A High Pressure Raman Study of Calcium Molybdate. *J. Phys. Chem. Solids* **1995**, *56*, 1125−1129.

(69) Errandonea, D.; Manjon, F. J. Pressure Effects on the Structural and Electronic Properties of ABX4 Scintillating Crystals. *Prog. Mater. Sci.* **2008**, *53*, 711−773.

(70) Jagielski, J.; Thomé, L. Multi-Step Mechanism of Damage Accumulation in Irradiated Crystals. *Nucl. Instrum. Methods Phys. Res., Sect. B* **2008**, *266*, 1212−1215.